Localized Surface Plasmon Resonances in Aluminum Nanodisks

Christoph Langhammer,* Markus Schwind, Bengt Kasemo, and Igor Zorić

*Department of Applied Physics, Chalmers University of Technology,
412 96 Göteborg, Sweden*

ABSTRACT

The plasmonic properties of arrays of supported Al nanodisks, fabricated by hole−mask colloidal lithography (HCL), are analyzed for the disk diameter range 61–492 nm at a constant disk height of 20 nm. Strong and well-defined (UV–vis–NIR) localized surface plasmon resonances are found and experimentally characterized with respect to spectral peak positions, peak widths, total cross sections, and radiative and nonradiative decay channels. Theoretically, the plasmon excitations are described by electrostatic spheroid theory. Very good qualitative and quantitative agreement between model and experiment is found for all these observables by assuming a nanoparticle embedded in a few nanometer thick homogeneous (native) aluminum oxide shell. Other addressed aspects are: (i) the role of the strong interband transition in Al metal, located at 1.5 eV, for the plasmonic excitations of Al nanoparticles, (ii) the role of the native oxide layer, and (iii) the possibility of using the plasmon excitation as an ultrasensitive, remote, real-time probe for studies of oxidation/corrosion kinetics in metal nanoparticle systems.

Studies of optically excited coherent conduction electron oscillations in metallic nanoparticles, known as localized surface plasmon resonances (LSPR), were for many years focused on the Ag and Au systems because of the favorable bulk dielectric properties of these metals.[1] Motivated by exciting prospects of combining nanoplasmonic activity with interesting intrinsic material properties found in other metals than Au and Ag, the plasmonic properties of novel materials have lately received more attention.[2–8] Today, it is generally accepted that the spatial constraint on the conduction electrons within a nanoparticle gives rise to tunable LSPRs even in metallic systems with less favorable bulk dielectric properties like Pt and Pd or Ni[2,6,7] or systems prone to surface oxidation like Cu.[4,5]

These findings suggest that many more metallic systems can support spectrally tunable LSPRs when in nanoparticle form. The essential difference between the "traditional" plasmonic materials (Au, Ag) and "novel" ones (like Pt, Pd) is basically to be found in the optical cross-section, the line width/dephasing time, and the dominating decay mechanism of the respective LSPR excitations.[3] All plasmonic systems have in common that their resonance energy is predominantly determined by the geometry and size of the metallic nanoparticle, its dielectric environment, and, but only to some extent, by the (real part of the) dielectric function of the metal. The global LSPR line width/dephasing time response is, on the other hand, predominantly determined by the imaginary part of the dielectric function

of the respective metal together with the particle size. The LSPR dephasing time is determined by the following mechanisms: pure dephasing due to elastic scattering of conduction electrons, Landau damping via intraband and interband single electron–hole excitations, and radiation damping.[9] For nanodisk systems in the size range discussed in the present work, radiation damping and interband damping are the most significant contributions to the total damping. In Drude-like metals, with low interband activity below a threshold for interband transitions, like in Ag and Au, radiation damping is most important, while in metals with sizable interband activity like in Pt and Pd, interband damping through electron–hole excitations is the dominating channel for the LSPR damping/dephasing.[3]

As a consequence, in Ag and Au, LSPRs are well defined excitations with long dephasing times in the energy range below a threshold for strong s−d interband activity (2.4 eV for Au and 3.8 eV for Ag, respectively).[10] Photons with energies above the interband threshold predominantly excite electron–hole pairs because LSPRs are then very unstable toward the decay trough the former channel.

In contrast, the energy dependent dielectric functions of both Pd and Pt reflect the presence of overlapping s and d-bands at the Fermi energy, giving rise to continuous interband activity over the entire UV–vis−NIR spectral range.[11] This is the main reason for the observed efficient decay of the LSPR through the nonradiative electron–hole channel and the short LSPR dephasing time in these systems.[2,3]

---
* Corresponding author. E-mail: christoph.langhammer@fy.chalmers.se.

Out of many other interesting candidate metals for nanoplasmonics, Al represents an interesting system both from a fundamental and an applications point of view (Al is, e.g., an abundant and cheap material compared to the noble metals). Its expected nanoplasmonic properties may in some sense "combine" some of the properties of the two classes of plasmonic materials discussed above.[1] A reasonably strong interband transition in Al[12] is localized in a narrow energy range around 1.5 eV and attributed to transitions between a pair of parallel bands around the Σ axis on the Γ−K−W−X plane. Below and above this energy, the interband activity is weak and Al is very much Drude-like.[13] Thus it is reasonable to expect that Al nanoparticles support long-lived LSPRs with high optical cross-sections and that these excitations are tunable over a wide energy range, deep into the UV. It is only in the narrow energy interval around the interband transition at 1.5 eV, where stronger damping (and thus decreased LSPR dephasing times) can be expected through interband transitions to electron–hole pairs.

From an applications point of view, Al nanoparticles potentially constitute an excellent model system, where intrinsic LSPRs might be utilized as a real-time and in situ probe to study oxidation (thermal, anodic, ...) processes and kinetics on the nanoscale under various conditions (gas or liquid environment, corrosive environment, etc.). In contrast to a recently introduced novel nanoplasmonic sensing scheme, relying on changes of the particle bulk dielectric properties during metal hydride formation,[14] the sensing process in the approach presented in this work is based on two different inherent properties of LSPRs. The first one is the high LSPR sensitivity to refractive index changes in the vicinity of the nanoparticle (widely used in a number of nanoplasmonic biosensing applications[15–24]), and the second one is the high sensitivity to size and shape changes of the particles. It is expected that a growing oxide shell is changing the dielectric properties of the nanoparticle environment and thus redshifting the LSPR energy while, at the same time, a metallic core, which shrinks in volume as the oxide grows, should give rise to a spectral blue-shift. The sum of these two contributions renders the total detected LSPR signal.

The primary goal of the work, presented in the first part of this letter, is to study and quantify the nanoplasmonic properties (LSPR energy, dephasing/lifetime, total cross-section, and contribution of scattering and absorption of light to the latter) of Al, with supported nanodisks as the model system. The influence of the native oxide layer on above-mentioned LSPR properties is an integral part of this study. In the second part of this letter, we therefore address the native oxide layer formation more in detail and show, in a proof-of concept approach, the applicability of LSPRs as ultrasensitive probes for studies of such processes. More extensive and detailed results from applying the LSPR for studying Al nanoparticle oxidation processes and kinetics in controlled environments will be part of a forthcoming publication.

The above issues are addressed experimentally and theoretically for Al nanodisks with average diameter D ranging from 61 to 492 nm and a height $h = 20$ nm, fabricated by the hole−mask colloidal lithography method (HCL)[25] on a transparent support (Borofloat glass, Schott Scandinavia AB). In contrast to ref 25, the lift-off step was carried out in ethylacetate (HPLC grade, Fisher Scientific) due to the higher solubility of PMMA in the latter and the lower water content as compared to acetone, which is commonly used for lift-off during HCL fabrication. The Al was evaporated in an electron beam evaporation system, at a base pressure of about 2×10^{-7} Torr and at a rate of approximately 2 Å/s. This nanofabrication method yields a partly random distribution of nanodisks on a substrate which, combined with a sufficiently large particle–particle separation, eliminates both far- and near-field optical coupling, i.e., the measured optical properties reflect a single-particle optical response.[2] The measured optical properties include the extinction, scattering, and absorption coefficients of the nanodisks. The former were obtained from direct measurements of the extinction (in transmission mode) and absorption coefficients (using an integrating sphere accessory Varian DRA 2500 with a sample center mount for transflectance measurements) with a Varian Cary 5000 spectrophotometer, while the scattering coefficient was obtained by relying on the optical theorem.[26] In a typical integrating sphere experiment (see Figure 4a for a schematic drawing), the transparent sample is mounted in the center of the integrating sphere detector, at a 9° angle from the normal to the incident light beam. This assures that the specular scattering contribution (backward scattering normal to the sample surface, marked "S" in Figure 4a) is collected by the detector and not leaving through the front aperture. Comparing the total scattering signal collected by the integrating sphere for the nanostructured sample with a reference (Labsphere Spectralon) yielding more than 99% reflectance in the spectral range between 350 and 1800 nm and more than 96% reflectance in the range between 200 and 2500 nm (6–0.5 eV) yields the absorption coefficient of the nanodisks on the sample. All the optical spectra were obtained within maximum 1 day after sample fabrication. The absolute cross sections for extinction, scattering, and absorption were calculated from the measured respective optical coefficients and the particle number density on the surface. The latter was obtained from scanning electron microscope (SEM) images of the nanostructures (Table 1), taken on a FEI Quanta 200 FEG ESEM at an acceleration voltage of 20 keV.

A theoretical description of the experimental system is made by approximating the metal disks with oblate spheroids, where, in the electrostatic limit, fully analytical solutions are available. For $D \ll \lambda$, in the quasistatic approximation, the oblate spheroid is treated as an individual dipole induced by an external field, parallel to the major axis of the spheroid. The dipolar–polarizability of the spheroid can then be expressed as[26,27]

$$\alpha(\omega) = \frac{\pi D^2 h}{6} \frac{\varepsilon_{Al}(\omega) - \varepsilon_m}{\varepsilon_m + L[\varepsilon_{Al}(\omega) - \varepsilon_m]} \qquad (1)$$

Here L is a geometric factor, which is determined by the ratio of the major axis (corresponding to the diameter of the disk D) and the minor axis (corresponding to the height of the disk h), and $\epsilon_{Al}(\omega)$ and ϵ_m are the dielectric functions of

Table 1. Summary of Important Parameters of the Fabricated Al Nanodisks[a]

nominal diameter [nm]	effective diameter [nm]	standard deviation [nm]	normalized std dev [%]	number density [μm^{-2}]	surface coverage [%]
51	61	4.8	7.87	24.6	7.31
76	78	5.1	6.54	16.4	7.98
110	104	5	4.8	9.62	8.2
120	115	4	3.48	8.7	9.12
140	136	4.5	3.3	6.05	8.75
170	157	3	1.91	5.37	10.4
190	175	4.7	2.68	3.55	8.61
250	262	5.6	2.14	2.14	11.6
300	288	6.6	2.29	0.954	6.24
530	492	22.9	4.65	0.359	6.82

[a] The nominal diameter corresponds to the mean diameter of the polystyrene spheres used during the fabrication process. The real diameter corresponds to the mean diameter of the Al nanodisks as determined from SEM image analysis after fabrication. The surface coverage, also obtained from SEM image analysis, is used to calculate the extinction, absorption and scattering efficiencies.

bulk Al and the embedding medium, respectively. For the embedding medium, an effective refractive index (n_{eff} = 1.26) is used, averaging the values of air (1.00) and the glass substrate (1.52).[2]

Because in this work a wide range of disk sizes is addressed, the quasistatic approximation has, for large D, to be corrected due to finite wavelength effects. The resulting corrected expression for the dipolar–polarizability can then be written as[28–30]

$$\alpha'(\omega) = \alpha(\omega)\left[1 - i\frac{k^3}{6\pi}\alpha(\omega) - \frac{k^2}{2\pi D}\alpha(\omega)\right]^{-1} \quad (2)$$

Here k is the wave-vector of the incident light. The k^3 term in eq 2 accounts for a radiation damping contribution, and the k^2 term accounts for dynamic depolarization. Note that retardation effects related to the variation of the E-field amplitude over the particle as well as delays in the electron gas response to the external field are not included in eq 2. On the basis of modified polarizability, the extinction and scattering efficiencies can be obtained

$$Q_{ext}(\omega) = \left[\pi \cdot \left(\frac{D}{2}\right)^2\right]^{-1} \cdot k\,\text{Im}[\alpha'(\omega)] \quad (3)$$

$$Q_{sca}(\omega) = \left[\pi \cdot \left(\frac{D}{2}\right)^2\right]^{-1} \cdot \frac{k^4}{6\pi}|\alpha'(\omega)|^2 \quad (4)$$

The absorption efficiency, based on the optical theorem,[26] can be expressed as

$$Q_{abs}(\omega) = Q_{ext}(\omega) - Q_{sca}(\omega) \quad (5)$$

Within electrostatic spheroid theory, in the quasistatic limit, a homogeneous oxide layer can be accounted for by modifying the expression for the dipolar–polarizability $\alpha(\omega)$ and by introducing a dielectric shell around the oblate spheroid. This then reads as[26]

$$\alpha''(\omega) = \frac{\pi D^2 h}{6} \cdot (\varepsilon_{Alox}(\omega) - \varepsilon_m) \cdot [\varepsilon_{Alox}(\omega) + (\varepsilon_{Al}(\omega) - \varepsilon_{Alox}(\omega)) \cdot ((L_i) - f \cdot L_o)] + f \cdot \varepsilon_{Alox}(\omega) \cdot (\varepsilon_{Al}(\omega) - \varepsilon_{Alox}(\omega))/[\varepsilon_{Alox}(\omega) + (\varepsilon_{Al}(\omega) - \varepsilon_{Alox}(\omega)) \cdot (L_i - f \cdot L_o)] \cdot [\varepsilon_m + (\varepsilon_{Alox}(\omega) - \varepsilon_m) \cdot L_o] + f \cdot L_o \cdot \varepsilon_{Alox}(\omega) \cdot (\varepsilon_{Al}(\omega) - \varepsilon_{Alox}(\omega)) \quad (6)$$

L_i is the geometric factor of the *inner* spheroid (the metallic core) and L_o is the geometric factor of the *outer* spheroid (metallic core plus dielectric shell), which is determined by the ratio of the major and minor axes of the respective

spheroids. D and h correspond to the diameter and height of the *outer* spheroid, respectively. The factor f corresponds to the fraction of total particle volume occupied by the *inner* spheroid. $\varepsilon_{Al}(\omega)$ is the frequency dependent dielectric function of an oxide-free Al thin film evaporated at room temperature,[31] $\varepsilon_{Alox}(\omega)$ is the dielectric function of aluminum oxide Al_2O_3,[32] and ε_m the dielectric constant of the surrounding medium. As above, an effective refractive index (n_{eff} = 1.26) is used for the surrounding medium. To account for radiation damping and dynamic depolarization, this extended expression of the dipole polarizability for a metal spheroid with a dielectric shell is substituted into eq 2 for the dipole polarizability of the oblate spheroid.

In parts a and b of Figure 1, SEM micrographs of typical arrays of Al nanodisks, fabricated with HCL, are shown for average particle diameters D = 61 nm and D = 115 nm. As reported earlier,[2,25] the surface coverage varies significantly for different disk diameters (Table 1). As another important property of HCL structures, the polydispersity in the particle size distribution should be mentioned. The latter effect is significant for small particle sizes (compare the structures in parts a and b of Figure 1 and see Table 1) and causes an additional inhomogeneous broadening of the LSPR line width.[33] Figure 1c shows a tapping mode atomic force microscope (AFM, Digital Instruments Dimension 3000 scanning probe microscope) scan of a single 288 nm Al disk. The 3D plot of the obtained topography image, together with a line scan, reveals a disk with a rather rough surface ($R_a \approx$ 4 nm). This roughness is predominantly determined by the oxide growth and to a lesser degree by the Al film growth process during evaporation.

Figure 1d shows measured extinction efficiencies (extinction cross section in units of nanodisk geometric area) for Al nanodisks with diameters D varying from 61 to 492 nm as a function of photon energy. As expected, a pronounced peak in extinction efficiency, associated with excitation of the dipolar LSPR, is spectrally red-shifting with increasing disk diameter due to the dependence of the LSPR energy on aspect ratio (and volume).[2] In addition, its full width at half-maximum (fwhm) decreases with increasing disk size. As for Pt, Pd, Ag, and Au nanodisks,[2,3] the resonances are located in the UV–vis−NIR spectral range. An additional feature, located always at 1.5 eV, is clearly observed for 157, 136, 115, and 104 nm Al nanodisks to the "left" (lower
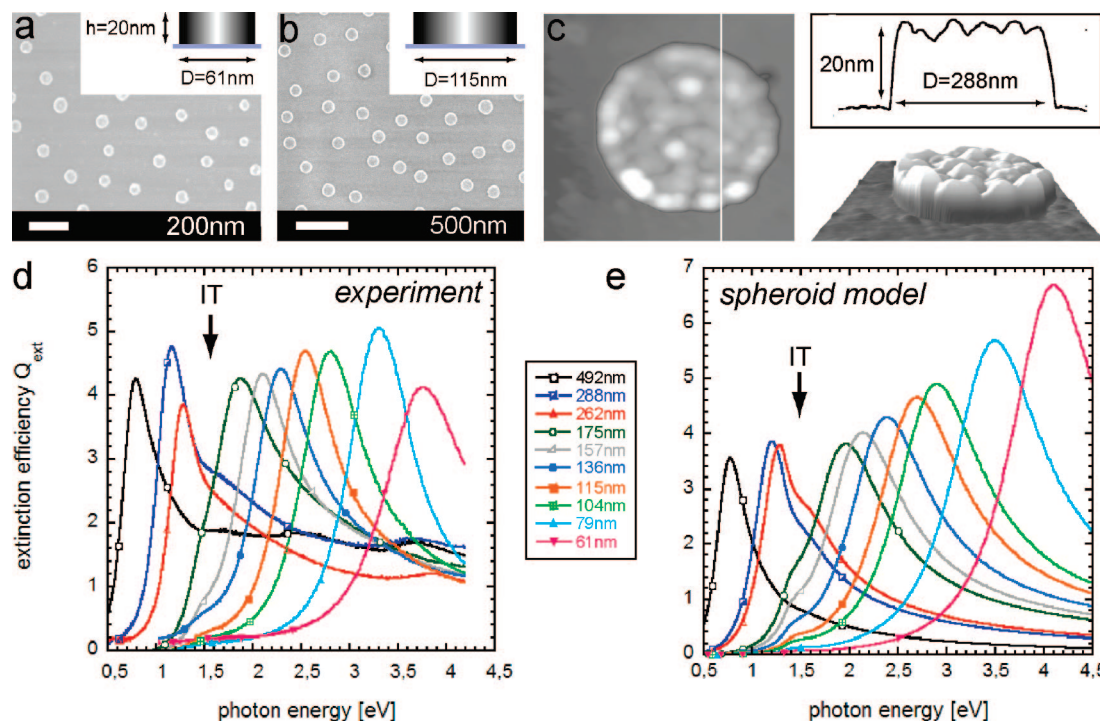
Figure 1. SEM micrographs of Al nanodisks with a mean diameter (a) $D = 61$ nm and $h = 20$ nm and (b) for $D = 115$ nm and $h = 20$ nm. (c) AFM scan of a single $D = 288$ nm Al nanodisk. The 3D image and the line scan reveal a rather rough surface with pronounced grainy microstructure. (d) Measured extinction efficiencies for Al nanodisks for a range of disks diameters 61 nm $< D <$ 492 nm at constant height $h = 20$ nm. A pronounced peak in extinction efficiency, associated with excitation of the dipolar LSPR, is spectrally red-shifting with increasing D. An additional feature, located always at 1.5 eV (marked with IT and black arrow in the figure) is observed in the spectra and can be associated with the interband transition in Al metal. For $D = 262$, 288, and 492 nm, respectively, one, two, and three additional peaks can be seen on the high-energy side of the dipolar resonance. (e) Calculated dipolar spheroid theory extinction spectra for the same D range as in the experiment. All experimentally observed dipolar LSPR and interband transition features are very nicely reproduced by the model, both qualitatively and quantitatively. The reason for the discrepancy in extinction efficiency between experiment and model calculation for $D = 61$ nm is a direct consequence of the polydisperse particle size distribution.

energy side) of the dipolar LSPR peak. For 79 and 61 nm disks, the former feature is also present but is much weaker and not clearly visible in Figure 1 because of the used extinction efficiency scale. This feature can be associated with the mentioned interband transition in Al metal.[12] For larger Al nanodisks, the interband transition peak appears as a shoulder centered at 1.5 eV to the "right" (higher energy) of the dipolar LSPR peak. Furthermore, for diameters of 262, 288, and 492 nm, respectively, one, two, and three additional peaks can be seen on the high-energy side of the dipolar resonance peak. These peaks are attributed to higher modes of the plasmon oscillation (quadrupole, octapole, and hexa-decapole), when well separated from the interband transition at 1.5 eV. In cases ($D = 262$, 288, and 492 nm) when the lowest energy additional peak is located close to 1.5 eV, its nature may be more complicated because of the coupling between the interband transition and an adjacent higher plasmon mode. It is worth noticing that the higher mode peaks are broader for Al than the corresponding ones in Ag and Au nanodisks.[3] The possible reason can be found in the higher conduction electron density in Al, leading to a larger radiation damping and peak broadening. Obviously, this reasoning should apply also to the width of the dipolar mode. A comparison with reported data for Ag and Au nanodisks of the same size[3] confirms these trends. The absolute

extinction efficiency values are found to be comparable to those of Ag and Au nanodisks.[3]

In Figure 1e, calculated extinction spectra from the spheroid model are shown for the disk diameters used in the experiments. All dipolar LSPR and interband transition features observed in the experimental spectra are very nicely reproduced by the model, both qualitatively and quantitatively, except for the smallest disks with $D = 61$ nm, where a significantly lower extinction efficiency is found in the experiment compared to theory. This difference is a direct consequence of the polydisperse particle size distribution, very pronounced for these small disks (clearly seen in the SEM image in Figure 1a). The broad size distribution leads to a broadening of the measured resonance peak and a decrease of the peak maximum.

For further quantification and (theoretical) analysis of the experimental results, at this point, the fact that Al forms a stable oxide (Al_2O_3) immediately after exposure to laboratory environment during the sample preparation process,[34] must be taken into account because it is expected to significantly alter the plasmonic response. The relative importance of this effect is expected to increase with decreasing particle size. Angle resolved X-ray photoelectron spectroscopy (XPS, Mg Kα radiation at 1253.6 eV) analysis of 20 nm Al thin films (see Supporting Information for details), evaporated under
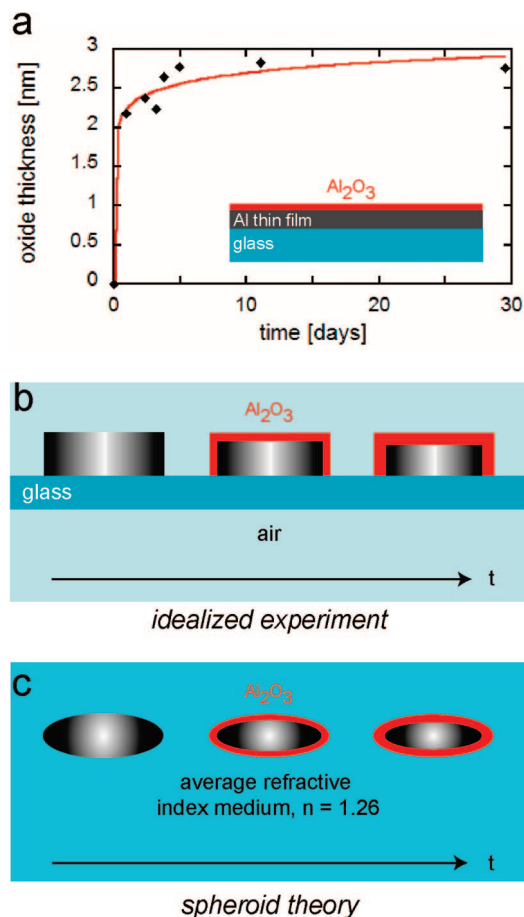
Figure 2. (a) Angle resolved X-ray photoelectron spectroscopy (XPS) analysis of 20 nm Al thin films, evaporated under the same conditions as in the nanodisk fabrication. The native oxide layer thickness is found to be of the order of 2.5–3 nm and forms within a few hours after air exposure. The red solid line represents a direct logarithmic fit to the XPS data. (b) Schematic depiction of the oxidation process in the supported Al nanodisks used in the experiment. It is assumed that a homogeneous oxide layer is formed around the particle surfaces that are exposed to ambient environment, while no oxidation takes place at the glass−Al interface. The oxide thickness is increasing with time. (c) Schematic depiction of how the oxidation process is modeled in spheroid theory. It is assumed that the total volume of the spheroid is not changing, i.e., that the metal core is shrinking on the cost of a growing homogeneous oxide layer. The spheroid is embedded in an average refractive index medium with a refractive index $n = 1.26$, corresponding to the average between air ($n = 1$) and glass ($n = 1.52$).

the same conditions as in the nanodisk fabrication, shows that a native oxide with a thickness of 2.5–3 nm is formed within a few hours after air exposure (Figure 2a). The red solid line in Figure 2a represents a direct logarithmic fit to the XPS data.

In an idealized and somewhat simplified picture, this oxidation process for supported Al nanodisks can be described as depicted schematically in Figure 2b. There, after metal evaporation, the Al nanodisk sitting on a glass substrate starts forming a homogeneous oxide shell at the cost of a shrinking metal core (the total volume of the particle is kept constant in the modeling, an assumption not absolutely correct in reality because Al_2O_3 has a slightly lower volume

density compared to Al metal,[34] but justified for the present purpose as it significantly simplifies the theoretical treatment). In a more realistic picture, the oxidation process as well as the chemical composition and the resulting microstructure are far more complex.[35,36]

Extending the introduced spheroid model by introducing a homogeneous oxide shell, as formally described above and depicted schematically in Figure 2c, thus facilitates a further and more detailed analysis of the experimental extinction spectra. In the model description, it is assumed (for simplicity, as discussed above) that the total diameter D and height h of the spheroid remain unchanged upon oxidation (i.e., that only the metal core "shrinks" homogeneously to a diameter D_{core} and height h_{core} by a factor $2d$, where d is the oxide shell thickness and that neither cracks nor aluminum hydroxide are formed).

In Figure 3a, calculated extinction spectra are displayed for three different disk sizes ($D = 61$, 136, and 288 nm) for three different modeling situations. The solid black lines represent calculated spectra for nonoxidized pure Al spheroids with long axes corresponding to the experimental disk diameters D and short axis corresponding to the experimental disk height $h = 20$ nm. The dashed black lines are calculated spectra for spheroids consisting of nonoxidized pure Al but with dimensions corresponding to the "metal core" of an oxidized spheroid with an oxide thickness $d = 3$ nm (i.e., long axis $D_{core} = D - 2d = 55$, 130, and 282 nm, short axis $h_{core} = h - 2d = 14$ nm). The dashed dark-blue lines, finally, correspond to the extinction spectra of spheroids with an oxide shell with thickness $d = 3$ nm (the difference between the two last cases thus lies in the value of the dielectric constant in the volume closest to the Al particle, corresponding to the oxide shell). These spectra qualitatively show very clearly that the relative effect of an oxide shell of constant thickness on the LSPR is inversely proportional to the nanodisk size. A more detailed analysis follows below. As characterization parameters for both calculated and the experimental extinction spectra, the LSPR energy, the full width at half-maximum (fwhm), and the peak value of the extinction efficiency are chosen. The LSPR energy is obtained by taking the first derivative of a fitted polynomial function to the experimental spectra as described by Dahlin et al.[37] To determine the fwhm of the asymmetric LSPR peaks, the width of half the peak, from the resonance maximum toward the lower energy side, is multiplied with a factor 2 to exclude higher plasmonic mode contributions.

In Figure 3b, the red triangles show the experimentally obtained D-dependence of the LSPR energy/peak position (in eV). If plotted as a function of LSPR wavelength (in nm) the peak position is scaling linearly with the diameter D (not shown here), as also found earlier for Pt, Pd, Ag, and Au nanodisks.[2,3] The solid black line in the same figure complies with the prediction from the spheroid model, calculated for a pure Al metallic nanodisk. A reasonably good agreement between the theoretical prediction and experimental data is obtained, in particular for larger nanodisks, while a systematic deviation occurs and becomes more pronounced, as the nanodisks get smaller. This deviation can
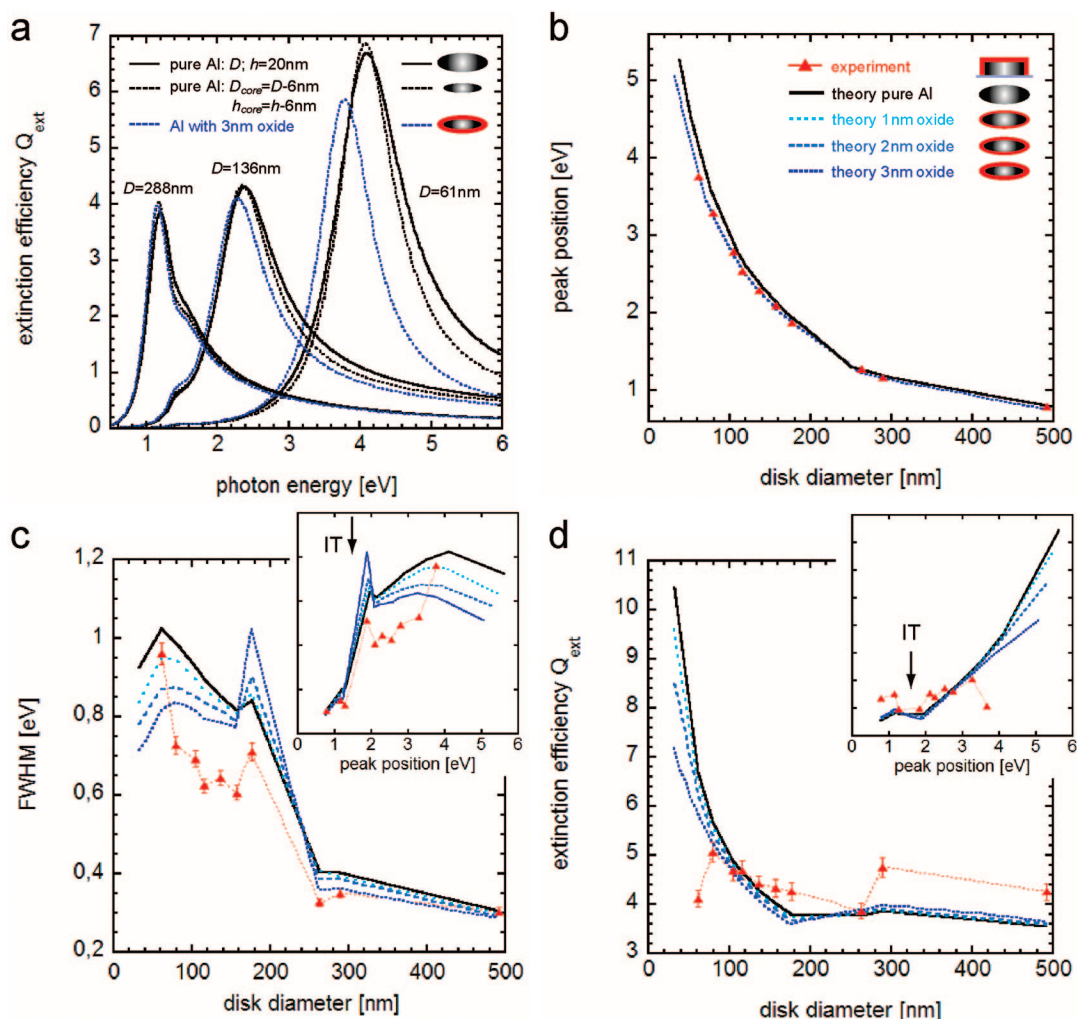
Figure 3. (a) Calculated extinction spectra for disks with $D = 61$ nm, $D = 136$ nm, and $D = 288$ nm. The solid black lines represent calculated spectra for unoxidized pure Al spheroids with long axes corresponding D and short axis $h = 20$ nm. The dashed black lines are calculated spectra for spheroids consisting of unoxidized pure Al but with dimensions corresponding to the "metal core" of an oxidized spheroid with an oxide thickness $d = 3$ nm (i.e., long axis $D_{core} = D - 2d = 55$, 130, and 282 nm, short axis $h_{core} = h - 2d = 14$ nm). The dashed dark-blue lines correspond to the extinction spectra of spheroids with an oxide shell with thickness $d = 3$ nm. (b) Experimentally obtained D-dependence of the LSPR energy/peak position (red triangles). The solid black line shows the spheroid model calculation for pure Al metallic nanodisks, and the dashed dark-blue line the calculation with a 3 nm thick oxide shell. The error bars for the experimental data points, obtained from measurements of different sample series, are of the order of the used symbol size. (c) Experimentally obtained values of the fwhm of the dipolar peak as a function of disk diameter (red triangles). The maximum in fwhm for nanodisks with $D \approx 200$ nm is attributed to the interband transition at 1.5 eV (see inset), giving rise to stronger damping of the LSPR through decay into e–h pairs. The solid full black line corresponds to the fwhm calculated with spheroid theory for pure Al, while the blue dashed lines correspond to spheroids with oxide shells of 1, 2, and 3 nm thickness, respectively. (d) Scaling of the extinction efficiency Q_{ext} at dipole peak maximum with disk diameter (and peak position in the inset) for the experiment (red triangles), spheroid theory for pure Al (black solid line) and spheroids with increasing oxide thickness (blue dashed lines). In (c) and (d) the error bars indicate the spread in the obtained data based on measurements on different sample series.

be understood and accounted for by introducing an aluminum oxide shell in the spheroid model, as described above. Three oxide shell thicknesses are introduced in our calculations: 1, 2, and 3 nm. As can be seen for an oxide shell of 3 nm thickness, a very good agreement between the model prediction and the experiment is obtained. This thickness is in good agreement with experimentally reported thicknesses of native oxide layers on Al surfaces[34] as well as with our own XPS measurements on 20 nm Al films. The observed larger relative effect of the oxide shell on the LSPR energy for small disks can be understood in the following way. As seen from the calculated spectra in Figure 3a, the change of

the volume and aspect ratio (D/h) of the metallic core due to shrinkage only, has a minor effect on the LSPR energy. It is the presence of the high refractive index oxide layer that induces the spectral red-shift of the LSPR energy, with the absolute resulting shift being related to the decay length of the enhanced electric field ("sensing volume") around the nanodisk and the spatial extension of the latter with respect to the oxide layer thickness. This issue will be discussed in more detail at the end of the article.

In Figure 3c, the red triangles show the experimentally obtained values of the fwhm of the dipolar peak of the LSPR (inversely proportional to the LSPR dephasing time) as a

function of disk diameter. A general trend of decreasing fwhm for increasing D is found. In addition, a maximum in fwhm for nanodisks with $D \approx 200$ nm is observed. For these particular D values, the LSPR energy is located around 1.5 eV in the region of the interband transition in Al (see inset in Figure 3c). This increased fwhm is a consequence of a stronger damping channel of the LSP excitation through decay into e−h pairs at this energy, promoted by the accessibility of interband transitions between parallel bands. Again, the solid black line in Figure 3c corresponds to the fwhm calculated with spheroid theory for pure Al, while the blue dashed lines correspond to spheroids with oxide shells of 1, 2, and 3 nm thickness, respectively. Good qualitative agreement with the experiment is found, except that the theoretical curves all show a maximum for $D \approx 60$ nm, while a monotonous increase in the fwhm is found in the experiment. This discrepancy can again be explained by the polydispersity in the disk size distribution, introducing inhomogeneous broadening for the smallest D. The observed decrease of the fwhm for increasing thickness of the oxide shell can almost entirely be attributed to the reduction of the size/volume of the metal core of the nanodisk, not the oxide itself. Qualitatively this becomes clear from the examples of calculated spectra shown in Figure 3a. We also want to point out that globally, the fwhm values obtained from the experiment are lower than the ones obtained with spheroid theory calculations. This is, at the first sight, rather surprising. However, as it becomes clear from the trends in Figure 3c, when increasing the oxide layer thickness, the agreement between experiment and theory is improving due to the shrinking core effect. Obviously, by increasing the thickness of the oxide shell in the model even further, one would be able to reproduce the experiment quite nicely. We chose, however, not to do that because, in view of the rather simple modeling of the rather complex real oxide shell formation, it is very likely that some of the observed discrepancy in fwhm is due to shortcomings of the model, as discussed later in the text.

Finally, Figure 3d shows the scaling of extinction efficiency Q_{ext} at dipole peak maximum with disk diameter for the experiment (red triangles) and spheroid theory for pure Al (black solid line) and spheroids with increasing oxide thickness (blue dashed lines). The general trend is a more or less constant Q_{ext} for the diameter range 500 nm > D > 300 nm, corresponding to LSPR energies between 0.8 and 1.2 eV (see inset Figure 3d). For 300 nm > D > 190 nm, corresponding to LSPR energies between 1.2 and 1.8 eV, a minimum is found for Q_{ext}. For smaller disk diameters, Q_{ext} increases very strongly with decreasing D. This behavior is contrasting what is found for both the Ag and Au[3] and Pt and Pd[2,3] systems. In those cases, either a maximum in Q_{ext} is found for a specific D, in the range where the branching ratio between radiative and electron–hole LSPR decay is about 1 (Ag, Au), or Q_{ext} monotonously decreases with decreasing D (Pt, Pd: note that for these systems, the e−h decay always dominates), respectively. For the case of Al, the decreasing extinction efficiency for larger disks can be understood by an increasingly important contribution of

radiation damping in the system because the size of the dipole increases and thus its radiative power. The minimum in Q_{ext} in the energy range around 1.5 eV (see the inset in Figure 3d) is caused by increased e−h damping of the plasmon resonance, promoted by the accessibility of the interband transitions in this energy range. The reduced Q_{ext} for the smallest disks is again a consequence of the particle polydispersity. When comparing experimental data points with theory, a very good quantitative and qualitative agreement is found. The observed effect of an oxide shell is very small in the large disk size regime. For small disks, the oxide shell significantly reduces the extinction efficiency. As becomes clear from the calculated spectra in Figure 3a, this reduction is a direct consequence of the presence of the oxide and can not be explained by a "shrinking core effect". The latter would, in contrast, rather lead to increased extinction efficiency.

The energy stored in a coherent plasmonic oscillation of the conduction electrons of a metal nanoparticle is transferred during the decay process of the latter. Two decay channels are available, radiative decay through photon emission (scattering) and nonradiative decay through e−h excitation (absorption). The branching ratio between these two decay channels in metal nanodisks is strongly dependent on disk diameter/aspect ratio and particle material, as shown for Ag, Au, Pt, and Pd systems.[3] In Figure 4b, we show the energy dependence of the extinction (red line), scattering (green line), and absorption (blue line) efficiencies for Al nanodisks with diameters D ranging from 61 to 492 nm. A striking feature, in view of the known high reflectivity of Al films,[13] is the significant absorption contribution to the total extinction cross section for disks with D < 300 nm. For D < 100 nm, absorption becomes the dominant decay mechanism. The interband transitions around 1.5 eV (marked with a solid line arrow and "IT" in Figure 4b) manifests itself clearly by enhancing the nonradiative decay, as expected. This is very nicely represented as a clear break in the trend of increasing scattering contribution to the total cross-section for increasing D. In the D range supporting an LSPR excitation with energy close to the interband transition, i.e., 175 nm < D < 262 nm, the absorption contribution to the total cross-section transiently increases before decreasing strongly for $D = 288$ nm and $D = 492$ nm. For nanodisks with D > 140 nm, higher order plasmon modes are clearly visible (marked with dashed arrows and Q = quadrupole, O = octapole, and H = hexadecapole in Figure 4b). It appears that they contribute predominantly via scattering to the total cross section.

In Figure 5, the experimentally measured scattering and absorption spectra are further quantified and analyzed by the means of the spheroid model. Figure 5a shows a series of calculated scattering spectra for three different D values, representing the small ($D = 61$ nm) and large particle limit ($D = 288$ nm), as well as the intermediate ($D = 136$ nm) size range. For the three different sizes, as described above, spectra corresponding to three different modeling situations are presented in order to distinguish between oxide shell induced effects and "shrinking core" effects. It becomes clear that both the reduction of the metal core and the presence
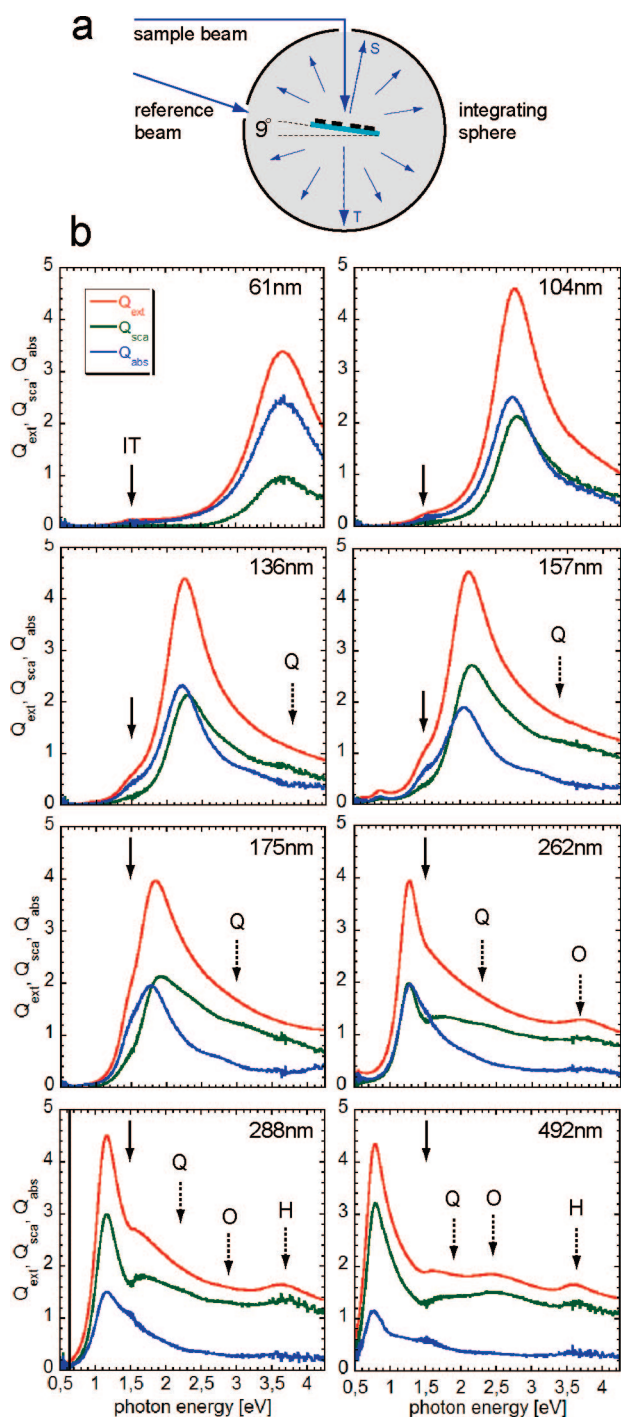
Figure 4. (a) Schematic depiction of an integrating sphere experiment. The sample is placed in the center, tilted 9° off the normal to the probing light beam to include the specular (backward) scattering component (marked "S"). (b) Extinction (red solid lines), scattering (green solid lines), and absorption (blue solid lines) efficiencies for Al nanodisks with increasing D. The interband transition feature at 1.5 eV (solid line arrow and "IT") manifests itself predominantly as an absorptive process. Its effect, enhanced e–h decay, is very nicely represented as weak break in the trend of the increasing scattering for increasing D. For $D > 175$ nm higher order plasmon modes are clearly visible (marked with dashed arrows and Q = quadrupole, O = octapole, and H = hexadecapole). Note that the higher modes predominantly scatter.

of an oxide shell have a significant effect on the scattering efficiency Q_{sca}. Both parameters reduce Q_{sca} by about the

same amount and the observed reduction is significant for small D (about 1.9 efficiency units for $D = 61$ nm), while it is almost negligible in the large D regime. The observed spectral red-shift of the scattering band of the LSPR when introducing the oxide shell is due to the higher refractive index of the oxide compared to air and glass.

Figure 5b shows calculated absorption efficiencies for the same conditions as described for Figure 5a. As can be seen, the reduction of the metal core leads to a significant increase of the absorption efficiency for all D. The increase is most pronounced for the smallest disks. Introducing an oxide layer does not, apart from the expected spectral red-shift, significantly alter the absorption efficiency. Note that the double peak structure for $D = 288$ nm is a consequence of a superposition/coupling of the absorption band of the LSPR and the interband absorption at 1.5 eV.

Comparing the theoretically obtained scattering efficiencies at dipole peak maximum for different oxide thickness with the experiment in Figure 5c shows generally good qualitative and improving quantitative agreement for increasing oxide thickness in the model. For 3 nm oxide, both the experimentally observed maximum in Q_{sca} for $D \approx 80$ nm and the minimum in Q_{sca} in the interband transition region, related to increased e–h decay, are well reproduced. As discussed above, the effect of both the oxide shell and the resulting shrinking metal core on Q_{sca} is most pronounced in the small disk diameter regime. For large D, the effect of the oxide on scattering efficiency is basically nonexistent, and the quantitative agreement between model and experiment is very good. Overall this implies that introducing an even thicker oxide layer in the spheroid model would improve the agreement in terms of the scattering efficiency. This would, however, also lead to a worse description of the spectral peak position and exceed the oxide thickness determined in the XPS experiments.

Figure 5d depicts the theoretically obtained absorption efficiencies Q_{abs} at dipole peak maximum for different oxide thickness together with the experimentally obtained values. As for the scattering efficiencies, good qualitative and improving quantitative agreement is found for increasing oxide thickness in the model. Nevertheless, we observe a significant offset between theory and experiment, covering the entire D range. For 3 nm oxide in the model, the offset is of the order of 0.6 efficiency units. The model is thus underestimating the absorption contribution to the total optical cross-section. Also here, introducing an even thicker oxide layer would improve the agreement between experiment and theory. In view of the excellent agreement between model and theory for the LSPR peak position for an oxide thickness of 3 nm and the fact that the XPS measurements on thin films confirm this oxide thickness, we chose not to do that. Instead, we want to point out other sources of uncertainty in the experiment as well as weaknesses of the model, to account for observed discrepancies and put the latter in the right perspective.

For the integrating sphere experiment, it is important to note that a small fraction of the scattered light is lost through the open sample and reference ports of the integrating sphere
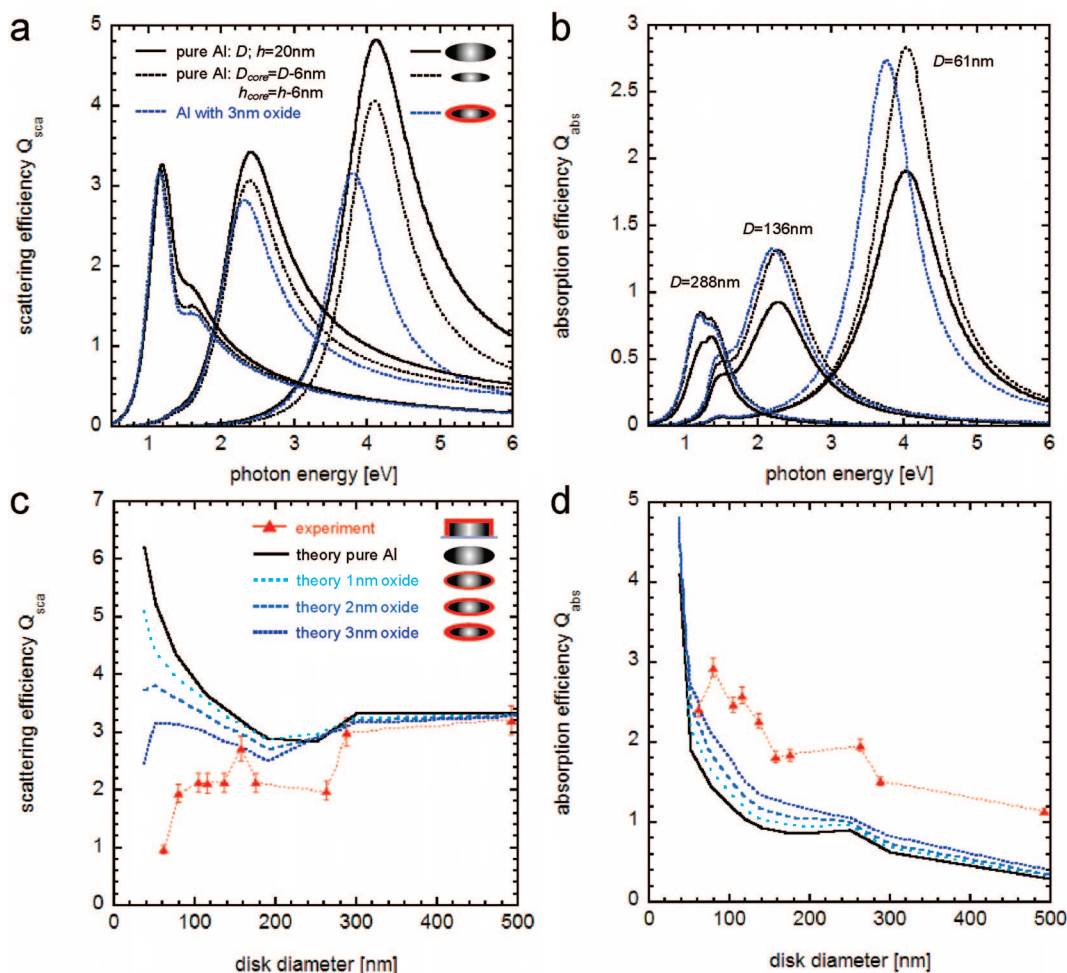
Figure 5. (a) Series of calculated scattering spectra for three different D values in the small ($D = 61$ nm) and large ($D = 288$ nm) particle limit, as well as the intermediate ($D = 136$ nm) size range. The solid black lines represent calculated spectra for unoxidized pure Al spheroids with long axes corresponding D and short axis $h = 20$ nm. The dashed black lines are calculated spectra for spheroids consisting of unoxidized pure Al but with dimensions corresponding to the "metal core" of an oxidized spheroid with an oxide thickness $d = 3$ nm (i.e., long axis $D_{core} = D - 2d = 55$, 130, and 282 nm, short axis $h_{core} = h - 2d = 14$ nm). The dashed dark-blue lines correspond to the scattering spectra of spheroids with an oxide shell with thickness $d = 3$ nm. (b) Calculated absorption efficiencies for the same conditions as described for (a). Note that the double peak structure for $D = 288$ nm is a consequence of a superposition of the absorption band of the LSPR and the enhanced interband absorption feature at 1.5 eV. (c) Comparison of the theoretically obtained scattering efficiencies at dipole peak maximum for different oxide thickness (solid and dashed lines) with the experiment (red triangles). Good qualitative and improving quantitative agreement is found for increasing oxide thickness in the model. (d) Theoretically obtained absorption efficiencies Q_{abs} at dipole peak maximum for different oxide thickness (solid and dashed lines) together with the experimentally obtained values (red triangles). As in (c), good qualitative and improving quantitative agreement is found for increasing oxide thickness in the model. Nevertheless, an offset between theory and experiment, covering the entire D range, is observed. Possible reasons are discussed in the text. In (c) and (d), the error bars indicate the spread in the obtained data based on measurements on different sample series.

(they cover, according to the specifications, approximately 7% of the sphere's inner surface), which leads to a slight underestimation of the measured scattering signal. To quantify these losses is very difficult because they strongly depend on the spatial distribution of the light scattered from the nanodisks where the latter again depends quite strongly on the particle size and shape. Some shortcomings of the spheroid model that was used should also be pointed out: (i) it only includes the dipolar plasmon mode, (ii) no substrate related effects are included in the calculations, (iii) the approximation of a nanodisk with an oblate spheroid leads to, e.g., significant differences in the particle volume between model and experiment, (iv) sharp edges like the rim of the disks, often associated with high local fields, are not present in the model, and (v) the surface of the spheroid is assumed

to be totally smooth and consist of a homogeneous metal without grain boundaries. The influence of surface roughness on the hybridized LSPR excitations in Au nanoshells was addressed both experimentally and theoretically (in FDTD calculations) by Halas and Nordlander et al.[38] and was shown to have a significant effect on the spectral peak position (red-shift/toward lower energies for increasing roughness and constant particle mass) and the LSPR dephasing/lifetime (increase for increasing roughness and constant particle mass) as well as extinction efficiency (increase for increasing roughness and constant particle mass). It may thus also be expected that surface roughness influences the scattering/absorption branching ratio.

In the second part of this article, we address the issue of stability of these Al nanostructures with respect to native
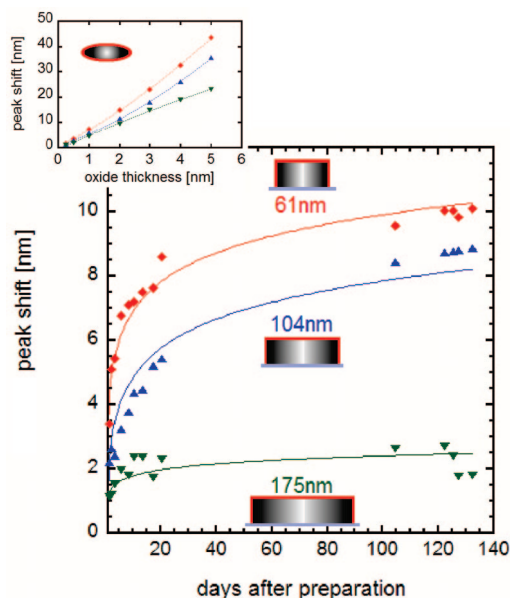
Figure 6. LSPR response of Al nanodisks with diameters $D = 61$ nm (red squares), 104 nm (blue triangles), and 175 nm (green inverted triangles) is plotted as a function of time exposed to controlled clean room environment ($T = 21 \pm 1$ °C, relative humidity $H = 43 \pm 3\%$) after evaporation and lift-off in organic solvent. The LSPR for all disk diameters exhibit a spectral red-shift with time upon oxide thickness increase, the latter being most pronounced for the smallest D. The solid lines represent direct logarithmic fits to the experimental data points. The inset shows the induced spectral LSPR shifts as a function of oxide layer thickness as calculated with spheroid theory for $D = 61$, 104, and 175 nm. The dashed lines are second-order polynomial fits to the calculated data points.

oxide formation under ambient conditions and their potential application as real time and highly sensitive probe for oxidation/corrosion kinetics studies. As mentioned in the text above, the formation of a thin 2−3 nm native oxide layer on an Al surface is almost instantaneous after its exposure to (humid) air. Typically, in humid air, in contrast to dry oxygen, the thickness of this layer continuously keeps increasing during several days or weeks, however, at orders of magnitude slower rate than the initial one. Because of the enormous technological importance of bulk Al and Al alloys, the surface oxidation of Al in (humid) air has been studied extensively over the years[39,40] and, as a consequence, a large number of theories and models for Al surface oxidation have been introduced.[34] It should also be pointed out here that surface oxidation is extremely sensitive to trace impurities and surface heterogeneities,[40] often making it very difficult to experimentally determine or confirm oxidation mechanisms suggested by theory. Nevertheless, the maybe most common model is the one developed long time ago by Cabrera and Mott,[41,42] recently also extended to the oxidation of nanometer-sized metal particles.[43] On the basis of the Cabrera−Mott theory for low temperature Al oxidation, both direct logarithmic and inverse logarithmic kinetics can be derived for slightly different oxidation mechanisms. In Figure 6, the LSPR response of Al nanodisks with diameters $D =$ 61 nm (red squares), 104 nm (blue triangles), and 175 nm (green inverted triangles) is plotted as a function of the time

of exposure to clean room environment ($T = 21 \pm 1$ °C, relative humidity $H = 43 \pm 3\%$). The LSPRs for all disk diameters exhibit a spectral red-shift with time, the latter being most pronounced for the smallest D. The observed, relatively large, scatter in the data points results from slight misalignments when repositioning the samples between measurements because the samples had to be moved between the clean room and the spectrophotometer. The solid lines in Figure 6 represent direct logarithmic fits to the experimental data points. The obtained agreement is very good for all D and in agreement with a study by Godard[39] on long-time, low-temperature oxidation of Al, observing direct logarithmic kinetics for oxidation in humid air in contrast to inverse logarithmic kinetics obtained in dry oxygen.

The observed larger spectral shift for smaller Al nanodisks, induced by the growing oxide layer, as seen in Figure 6, also needs to be addressed. As shown by Kobayashi et al.[44] for Au colloids, the spectral shifts induced by nanometer-thin layers of poly(methyl methacrylate) (PMMA) are larger for smaller colloids. This is due to a shorter decay length of the enhanced field around the nanoparticle and a resulting larger fraction of the "sensing volume" being occupied by the PMMA layer. Van Duyne et al. carried out experiments along the same lines, by depositing atomic layers of Al_2O_3 on triangular Ag nanoparticles[45] and self-assembled multi-layers based on the interaction of $HOOC\text{-}(CH_2)_{10}SH$ and Cu^{2+} on triangular Ag and Au nanoparticles.[46] They find, in contradiction to our results, as well as to the results for spherical Au colloids, larger LSPR shifts for particles with constant out-of plane height and increasing in-plane widths. This difference may, however, be explained by the very different nanoparticle geometry of truncated tetrahedrons and the role of the resulting enhanced field "hot-spots" at the tips of the tetrahedron[47] compared to the more symmetric nanodisk structures used in this work. The "sensitivity" to the increasing thickness of the oxide layer, i.e., the induced LSPR spectral shift, of the $D = 61$ nm Al nanodisks is found to be comparable to what is found by Van Duyne et al. in the Al_2O_3 atomic layer deposition experiments on Ag tetrahedrons.[45] The inset in Figure 6 shows the induced spectral shifts as a function of oxide layer thickness as calculated with spheroid theory for $D = 61$, 104, and 175 nm. The agreement with the experiment is excellent in terms of the observed increasing peak shifts for smaller D. Quantitatively, for the peak shifts obtained in the experiment after 140 days, the model predicts (assuming the presence of 2.5 nm oxide as starting point for the long-time oxidation experiment) a corresponding increase of the oxide layer thickness of about 1 nm for $D = 61$ and 104 nm and of about 0.5 nm for $D = 175$ nm, respectively. Having in mind that, during the particle fabrication process, a first native oxide layer of about 2.5 nm is formed almost immediately (as shown by the XPS measurements), this implies a resulting total oxide layer thickness of 3−3.5 nm after 140 days in humid air, which is very reasonable.[34] Note also the different scaling of the peak shift vs oxide layer thickness for 61 and 104 nm disks compared to the 175 nm disk. While for the first two, a positive second-order polynomial nicely describes

the data points shown in the inset, a negative second-order polynomial fit is needed for the 175 nm disk to describe the data from the spheroid model. A (somewhat speculative) explanation for this observation is related to the fact that the LSPR for a 175 nm disk is located very close to the interband transition, leading to enhanced e−h damping of the plasmon resonance and thus lower field enhancement around the nanodisk.

In conclusion, we have shown that Al nanodisks support strong, long-lived LSPR excitations that are tunable over the entire UV–vis−NIR spectral range by adjusting the disk diameter. Their total optical cross-sections are comparable to Au and Ag nanostructures of the same geometry, which makes Al nanoparticles a highly interesting cheap alternative to noble metal nanostructures in (potential) LSPR application areas like, e.g., plasmon enhanced photovoltaics.[48] The energy, dephasing times, and decay channels of Al nanodisk LSPRs are well described within an electrostatic spheroid model, taking into account the presence of the thin native oxide shell surrounding the nanodisk. An enhanced instability of the LSPR toward interband e−h excitations, in the narrow energy range around 1.5 eV, is observed and related to specific band structure in bulk Al. Furthermore, we have shown how LSPR can be used for remote and sensitive monitoring of Al oxidation kinetics where the red-shift of the LSPR peak position during the oxidation is related to the oxide layer growth and analyzed successfully with electrostatic spheroid theory. The observed LSPR sensitivities to local changes in the refractive index close to the nanodisks are found to be comparable to Ag nanostructures of comparable dimensions.

Supporting Information Available: Angle-resolved X-ray photoelectron spectroscopy for oxide layer thickness determination. This material is available free of charge via the Internet at http://pubs.acs.org.

References

(1) Kreibig, U.; Vollmer, M. *Optical Properties of Metal Clusters*; Springer: Berlin, 1995.
(2) Langhammer, C.; Yuan, Z.; Zoric, I.; Kasemo, B. *Nano Lett.* **2006**, *6*, 833–838.
(3) Langhammer, C.; Kasemo, B.; Zoric, I. *J. Chem. Phys.* **2007**, *126*, 194702.
(4) Chan, G. H.; Zhao, J.; Hicks, E. M.; Schatz, G. C.; Van Duyne, R. P. *Nano Lett.* **2007**, *7*, 1947–1952.
(5) Wang, H.; Tam, F.; Grady, N. K.; Halas, N. J. *J. Phys. Chem. B* **2005**, *109*, 18218–18222.
(6) Cao, L. Y.; Barsic, D. N.; Guichard, A. R.; Brongersma, M. L. *Nano Lett.* **2007**, *7*, 3523–3527.
(7) Zhang, Y. Q.; Yu, J. L.; Niu, H. J.; Liu, H. F. *J. Colloid Interface Sci.* **2007**, *313*, 503–510.
(8) González-Díaz, J. B.; García-Martín, A.; Armelles, G.; Navas, D.; Vázquez, M.; Nielsch, K.; Wehrspohn, R. B.; Gösele, U. *Adv. Mater.* **2007**, *19*, 2643–2647.
(9) Heilweil, E. J.; Hochstrasser, R. M. *J. Chem. Phys.* **1985**, *82*, 4762–4770.
(10) Johnson, P. B.; Christy, R. W. *Phys. Rev. B* **1972**, *6*, 4370–4379.
(11) Weaver, J. H. *Phys. Rev. B* **1975**, *11*, 1416–1425.
(12) Lee, K.-H.; Chang, K. J. *Phys. Rev. B* **1994**, *49*, 2362–2367.
(13) Ehrenreich, H.; Philipp, H. R.; Segall, B. *Phys. Rev.* **1963**, *1*, 1918–1928.
(14) Langhammer, C.; Zoric, I.; Kasemo, B.; Clemens, B. M. *Nano Lett.* **2007**, *7*, 3122–3127.
(15) Nath, N.; Chilkoti, A. *Anal. Chem.* **2002**, *74*, 504–509.
(16) Okamoto, T.; Yamaguchi, I.; Kobayashi, T. *Opt. Lett.* **2000**, *25*, 372–374.
(17) Haes, A. J.; Van Duyne, R. P. *J. Am. Chem. Soc.* **2002**, *124*, 10596–10604.
(18) Sun, Y. G.; Xia, Y. N. *Anal. Chem.* **2002**, *74*, 5297–5305.
(19) Prikulis, J.; Hanarp, P.; Olofsson, L.; Sutherland, D.; Kall, M. *Nano Lett.* **2004**, *4*, 1003–1007.
(20) Haes, A. J.; Chang, L.; Klein, W. L.; Van Duyne, R. P. *J. Am. Chem. Soc.* **2005**, *127*, 2264–2271.
(21) Sherry, L. J.; Chang, S. H.; Schatz, G. C.; Van Duyne, R. P.; Wiley, B. J.; Xia, Y. N. *Nano Lett.* **2005**, *5*, 2034–2038.
(22) Wang, H.; Brandl, D. W.; Le, F.; Nordlander, P.; Halas, N. J. *Nano Lett.* **2006**, *6*, 827–832.
(23) Nehl, C. L.; Liao, H. W.; Hafner, J. H. *Nano Lett.* **2006**, *6*, 683–688.
(24) Larsson, E. M.; Alegret, J.; Kall, M.; Sutherland, D. S. *Nano Lett.* **2007**, *7*, 1256–1263.
(25) Fredriksson, H.; Alaverdyan, Y.; Dmitriev, A.; Langhammer, C.; Sutherland, D. S.; Zaech, M.; Kasemo, B. *Adv. Mater.* **2007**, *19*, 4297–4302.
(26) Bohren, C. F.; Huffman, D. R. *Absorption and Scattering of Light by Small Particles*; John Wiley & Sons: New York, 1983.
(27) Landau, L. D.; Lifshitz, E. M.; Pitaevskii, L. P. *Electrodynamics of Continous Media*, 2nd ed.; Pergamon: Oxford, 1984.
(28) Wokaun, A.; Gordon, J. P.; Liao, P. F. *Phys. Rev. Lett.* **1982**, *48*, 957–960.
(29) Meier, M.; Wokaun, A. *Opt. Lett.* **1983**, *8*, 581–583.
(30) Kelly, K. L.; Coronado, E.; Zhao, L. L.; Schatz, G. C. *J. Phys. Chem. B* **2003**, *107*, 668–677.
(31) Palik, E. D. *Handbook of Optical Constants of Solids*; Academic Press: San Diego, 1998.
(32) Palik, E. D. *Handbook of Optical Constants of Solids II*; Academic Press: New York, 1991.
(33) Hanarp, P.; Kall, M.; Sutherland, D. S. *J. Phys. Chem. B* **2003**, *107*, 5768–5772.
(34) Fromm, E. *Kinetics of Metal-Gas Interactions at Low Temperatures: Hydriding, Oxidation, Poisoning*; Springer: New York, 1998.
(35) Atkinson, A. *Rev. Mod. Phys.* **1985**, *57*, 437–470.
(36) Lawless, K. R. *Rep. Prog. Phys.* **1974**, *37*, 231–316.
(37) Dahlin, A. B.; Tegenfeldt, J. O.; Hook, F. *Anal. Chem.* **2006**, *78*, 4416–4423.
(38) Wang, H.; Goodrich, G. P.; Tam, F.; Oubre, C.; Nordlander, P.; Halas, N. J. *J. Phys. Chem. B* **2005**, *109*, 11083–11087.
(39) Godard, H. P. *J. Electrochem. Soc.* **1967**, *114*, 354–356.
(40) Lawless, K. R. *Rep. Prog. Phys.* **1974**, *37*, 231–316.
(41) Cabrera, N.; Mott, N. F. *Rep. Prog. Phys.* **1948**, *12*, 163–184.
(42) Popova, I.; Zhukov, V.; Yates, J. T. *Surf. Sci.* **2002**, *518*, 39–48.
(43) Zhdanov, V. P.; Kasemo, B. *Chem. Phys. Lett.* **2008**, *452*, 285–288.
(44) Okamoto, T.; Yamaguchi, I.; Kobayashi, T. *Opt. Lett.* **2000**, *25*, 372–374.
(45) Whitney, A. V.; Elam, J. W.; Zou, S. L.; Zinovev, A. V.; Stair, P. C.; Schatz, G. C.; Van Duyne, R. P. *J. Phys. Chem. B* **2005**, *109*, 20522–20528.
(46) Haes, A. J.; Zou, S. L.; Schatz, G. C.; Van Duyne, R. P. *J. Phys. Chem. B* **2004**, *108*, 109–116.
(47) Hao, E.; Schatz, G. C. *J. Chem. Phys.* **2004**, *120* (1), 357–366.
(48) Hägglund, K.; Zäch, M.; Kasemo, B. *Appl. Phys. Lett.* **2008**, *92*, 013113.

NL080453I